Discrete dynamics of light in an anti-parity-time symmetric photonic lattice in atomic vapors

Qingsong Yu, Jiaqi Yuan, Zhenzhi Liu, Ruidong He, Shun Liang, Yanpeng Zhang, [ID] and Zhaoyang Zhang* [ID]

Key Laboratory for Physical Electronics and Devices of the Ministry of Education & Shaanxi Key Lab of Information Photonic Technique, School of Electronic Science and Engineering, Faculty of Electronic and Information Engineering, Xi'an Jiaotong University, Xi'an 710049, China
*zhyzhang@xjtu.edu.cn

We demonstrate the realization of an anti-*parity-time (PT)*-symmetric photonic lattice in a coherent three-level Λ-type ^{85}Rb atomic system both experimentally and theoretically. Such an instantaneously reconfigurable anti-*PT*-symmetric photonic lattice is "written" by two one-dimensional coupling fields, which are arranged alternately along the *x* direction and can modulate the refractive index of the atomic vapor in a spatially periodic manner via controllable atomic coherence. By properly adjusting the relevant atomic parameters, the phase shift between two adjacent lattice channels occurs in the constructed non-Hermitian photonic system. Such a readily reconfigurable anti-*PT*-symmetric photonic lattice may open the door for demonstrating the discrete characteristics of the optical waves in periodic anti-*PT*-symmetric photonic systems.   © 2023 Optica Publishing Group

The formal equivalence between the optical paraxial wave equation and the quantum Schrödinger equation has proven that the optical systems can serve as a fertile ground to investigate the intriguing properties of non-Hermitian systems [1], particularly the parity-time (*PT*)-symmetric ones. These systems remain constant under the combined effects of parity and time-reversal operators. Thus, *PT*-symmetric optical systems require that the real part of the refractive index is an even function of the space, while its imaginary part is an odd one, i.e. $n(x) = n^*(-x)$ [2,3]. Another important feature of the *PT*-symmetric system is the phase-transition point, beyond which not only the eigenvalues but also the corresponding eigenvectors become the same [4,5]. Based on this property, a variety of novel phenomena and applications have been explored under the *PT*-symmetric optical system in the past decade, such as double reflection [6], nonreciprocal light propagation [7,8], power oscillations [9,10], and unidirectional invisibility [11], to name a few.

In recent years, an anti-*PT* symmetry has emerged as a new platform to investigate the non-Hermitian physics. Contrary to the *PT* symmetry, the optical systems satisfying anti-*PT* symmetry require $n(x) = -n^*(-x)$, namely, the real (imaginary) part of the refractive index should be odd (even) function of the space [12,13]. This characteristic reveals that anti-*PT*-symmetric

optical systems can be realized without the need of an optical gain [14]. Also, unlike *PT*-symmetric systems possessing real eigenvalues, the eigenvalues of anti-*PT*-symmetric systems are purely imaginary, which brings about surprising effects and extraordinary utilities [15], such as constant refraction [16], optical energy-difference conservation [17], coherent switch [18], and multimode phonon lasing [19].

Since the first experimental demonstration of anti-*PT*-symmetry in an optical system via flying hot atoms [20], the study of anti-*PT*-symmetric optical systems has been extended to optical fibers [21], coupled waveguides [18,22], and microcavity [16]. Very recently, a periodic anti-*PT*-symmetric optical lattice has been experimentally prepared in a thermal atomic system [23], which is assisted by the electromagnetically induced transparency (EIT) [24]. By taking advantage of the multiple tunable parameters of such system, the spectral characteristics have been studied, and the unidirectional reflectionless light propagation has been observed. However, the discrete transport behaviors (one of the most fundamental effects of periodical photonic structures) in anti-*PT*-symmetric optical lattices have not yet been experimentally explored.

In this Letter, we propose an experimental method to construct a one-dimensional anti-*PT*-symmetric photonic lattice under the EIT condition in a coherently prepared three-level Λ-type ^{85}Rb atomic configuration, which is excited by two standing-wave coupling fields arranged alternately (their bright fringes do not overlap with each other) along the *x* direction and one weak co-propagating probe field. In the experiment, the induced spatially periodic photonic lattice can satisfy anti-*PT*-symmetry under certain experimental parameters. The phase evolution of anti-*PT*-symmetric Hamiltonian under different non-Hermitian degrees is manifested by monitoring the relative phase shift between two adjacent lattice channels. Furthermore, we calculated the band structure of the constructed anti-*PT*-symmetric photonic lattice by using the plane wave expansion method, and the typical features in non-Hermitian systems are demonstrated. The experimental realization of such instantaneous adjustable anti-*PT*-symmetric photonic lattice may open the door to explore the underlying discrete dynamic characteristics of light in anti-*PT*-symmetric photonic lattices.

The experimental setup is shown in Fig. 1(a). The coupling beam E_c emitted from the external cavity diode laser (ECDL 1)
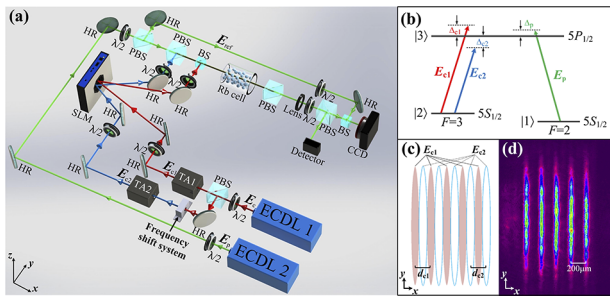
Fig. 1. (a) Experimental setup. The coupling beams E_{c1} and E_{c2} are both emitted from ECDL1 but with different frequencies, which is due to the presence of the frequency shift system for E_{c2}. These two coupling beams are both transformed into 1D periodic fields with the same periodicity by a SLM. The probe field E_p from ECDL2 is divided into two parts by a PBS: one part co-propagates with two coupling beams and its output diffraction pattern is imaged onto the CCD camera through an imaging lens, while the other part serves as a reference beam E_{ref} to generate the reference interference. ECDL, external cavity diode laser; $\lambda/2$, half-wave plate; TA, semiconductor tapered amplifier; HR, high-reflectivity mirror; SLM, spatial light modulator; PBS, polarization beam splitter; BS, beam splitter; detector, photodiode detector; CCD, charge-coupled device. (b) Three-level Λ-type ^{85}Rb atomic structure. (c) The spatial arrangement of two 1D coupling fields in ^{85}Rb cell, in which the periodicities d_{c1} and d_{c2} of the two coupling fields are both 200 µm. (d) Observed transmitted probe pattern on the CCD camera without E_{ref}.

is divided into two parts by a polarization beam splitter (PBS) together with a half-wave plate: one part directly enters the semiconductor tapered amplifier 1 (TA1) and serves as the coupling field E_{c1} (frequency ω_{c1}), while the other part enters the TA2 after being modulated by the frequency shift system and serves as another coupling field E_{c2} (frequency ω_{c2}). Here the frequency shift system consists of two acousto-optic modulators (AOMs): one AOM shifts the frequency of the laser with a frequency of 140 MHz, while the other AOM shifts the laser with a frequency ranging from −120 MHz to −160 MHz under the double-pass configuration. The frequency difference between two coupling fields can be tuned by varying the driven frequency of the double-pass AOM. By dividing the screen of the phase-controlled spatial light modulator (SLM) into two parts and loading appropriate phase holograms, the Gaussian coupling fields E_{c1} and E_{c2}, launched into the left and right halves of the SLM screen with an angle of about 6°, respectively, are modulated into one-dimensional (1D) periodic intensity profiles. The required hologram is calculated by the weighted Gerchberg–Saxton algorithm. The output two modulated coupling fields are set as vertical polarization and then sent into the atomic medium. The atomic vapor cell, with a diameter of 2.5 cm and a length of 3 cm, is packaged with a µ metal to shield the effect of external magnetic field and is heated to 363 K by a heat tape to provide appropriate atomic density. The weak Gaussian probe field E_p (frequency ω_p) from ECDL 2 co-propagates with the coupling fields and is incident into the vapor cell to detect the susceptibility profile of the medium. Consequently, a three-level Λ-type atomic structure shown in Fig. 1(b) is prepared to generate EIT, in which the probe field E_p drives the transition between the excited level $5P_{1/2}$ ($|3\rangle$) and the ground level $5S_{1/2}$, F = 2 ($|1\rangle$), while the two coupling fields E_{c1} and E_{c2} drive the same transition from another ground level $5S_{1/2}$,

F = 3 ($|2\rangle$) to $5P_{1/2}$ ($|3\rangle$) with different frequencies. The output wavelength of two ECDLs is ∼795 nm. Here, the frequency detuning Δ_p (Δ_{c1}, Δ_{c2}) is considered to be the difference between the laser frequency ω_p (ω_{c1}, ω_{c2}) and the natural frequency of the corresponding atomic energy levels. By setting the frequency detuning of the laser fields to satisfy the two-photon resonance condition $\Delta_p - \Delta_{c1} = 0$ ($\Delta_p - \Delta_{c2} = 0$), an EIT window with a spectral width of ∼30 MHz will occur. A PBS cube is placed behind the rear surface of the vapor cell to filter out the vertically polarized coupling fields, and only horizontally polarized probe field can be received by the capturing system. Then, the probe field is divided into two parts: one part is received by a charge-coupled device (CCD) camera to observe the spatial distribution of the output probe field, while the other part is injected into a photodiode detector to monitor the transmitted spectrum with EIT.

The spatial beam arrangement inside the ^{85}Rb vapor cell is depicted in Fig. 1(c), and the periodicity of two 1D coupling fields are the same ($d_{c1} = d_{c2} = 200$ µm). The fringes of two coupling fields are alternately arranged along the x direction, and the centers (along the x direction) of the bright fringe of E_{c1} and the dark fringe of E_{c2} overlap with each other. By elaborately controlling the frequency detuning to satisfy the condition $(\Delta_p - \Delta_{c1}) = -(\Delta_p - \Delta_{c2})$, two partially overlapped EIT windows will occur and an anti-*PT*-symmetric photonic lattice can be prepared; the output probe pattern is shown in Fig. 1(d). Further, we introduce a reference beam E_{ref} to interfere with the output probe field in the y direction to exhibit the phase shift between two adjacent bright and dark channels. Here, the E_{ref} is obtained from the same laser source as the probe beam, and they intersect at the plane of the CCD camera (see Fig. 1(a)). The current work adopts different experimental configurations from the atomic-coherence-based *PT*-symmetric photonic lattices [25–27], which employ the multi-beam interference method to generate periodic laser fields to drive a four-level atomic system with Raman gain.

Theoretically, the refractive index n in the atomic medium under the EIT condition can be expressed as $n = (1 + \chi)^{1/2} \approx 1 + \chi/2$. Meanwhile, considering $n = n_0 + \Delta n$, in which $n_0 = 1$ represents the background refractive index of the atomic gas, the variation of the refractive index caused by the EIT effect can be expressed as $\Delta n \approx \chi/2$. According to the density-matrix equations under the Λ-type energy-level atomic configuration, one can obtain the susceptibility $\chi = (2N\mu_{31}/E_p\varepsilon_0) \times \rho_{31}$ under the rotating-wave approximation [28], where N is the atomic density, ε_0 is the vacuum dielectric constant, and E_p is the electric-field intensity of the probe field E_p. μ_{31} and ρ_{31} are the dipole moment and the density-matrix element corresponding to the transition from $|1\rangle$ to $|3\rangle$, respectively. Thus, the spatially modulated susceptibility can be described as [29,30]

$$\chi = \frac{iN|\mu_{31}|^2/(\hbar\varepsilon_0)}{\left(\Gamma_{31} + i\Delta_p + \frac{|\Omega_{c1}|^2}{\Gamma_{32} + i(\Delta_p - \Delta_{c1})} + \frac{|\Omega_{c2}|^2}{\Gamma_{32} + i(\Delta_p - \Delta_{c2})}\right)}, \quad (1)$$

where Γ_{ij} is the decay rate between two states $|i\rangle \rightarrow |j\rangle$, $\hbar$ is the reduced Planck constant, and Ω_{c1} (Ω_{c2}) is the Rabi frequency of the coupling field E_{c1} (E_{c2}). Here, the Rabi frequency is defined as $\Omega_{c1(c2)} = \mu_{32}E_{c1(c2)}/\hbar$. According to Eq. (1), the distribution of the susceptibility can be effectively controlled by changing the parameters such as two-photon detuning and the Rabi frequency.
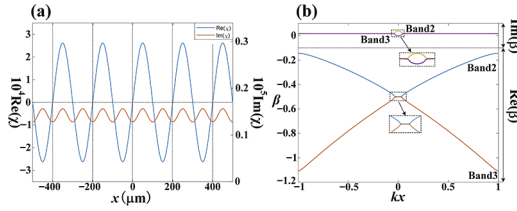
Fig. 2. (a) Theoretical calculation of the real (blue) and imaginary (red) parts of the susceptibility of the constructed anti-*PT*-symmetric photonic lattice under the frequency detuning $\Delta_{c1} = -6\,\text{MHz}$ and $\Delta_{c2} = 6\,\text{MHz}$ with $\Delta_p = 0$. (b) The real and imaginary parts of the band structure corresponding to the susceptibility are shown in (a). Other parameters used in the theoretical simulations: the atomic density $N \approx 5 \times 10^{14}\,\text{cm}^{-3}$, the Rabi frequency $\Omega_{c1} = \Omega_{c2} = 80\,\text{MHz}$.

Fig. 3. (a) Intensity ratio of the diffraction patterns under different $|\Delta_p - \Delta_{c1(c2)}|$. The blue solid curve is the theoretical prediction, and the red squares represent the experimental measured results. (b)–(d) Observed output diffraction patterns under the two-photon detuning $|\Delta_p - \Delta_{c1(c2)}| = 4$, 6, and 8 MHz, respectively.

Figure 2(a) shows the calculated spatial susceptibility of the constructed photonic lattice under $\Delta_{c1} = -\Delta_{c2} = 6\,\text{MHz}$ and $\Delta_p = 0$. One can clearly see that the real (imaginary) part of the susceptibility is an odd (even) function of position x, indicating that an anti-*PT*-symmetric lattice $\chi(z) = -\chi^*(-z)$ can be established in such atomic configuration under the condition $(\Delta_p - \Delta_{c1}) = -(\Delta_p - \Delta_{c2})$. In addition, to reveal the energy-momentum dispersion properties, we calculated the band structure of the constructed periodic anti-*PT*-symmetric photonic lattice with plane–wave expansion method [31], as shown in Fig. 2(b), from which the typical features in non-Hermitian systems can be observed. As marked by the dashed boxes, the degeneracy of band2 and band3 in Re(β) and the separation in Im(β) imply that the spontaneous symmetry breaking will occur when this region is excited.

With the anti-*PT*-symmetric photonic lattice is "written" in the atomic medium under the EIT condition, the propagation of the probe field in such a system is guided by the following Schrödinger-like paraxial equation [32]:

$$i\frac{\partial \psi(x,z)}{\partial z} + \frac{1}{2k_0}\frac{\partial^2 \psi}{\partial x^2} + \frac{k_0}{n_0}\Delta n(x)\psi = 0, \qquad (2)$$

where ψ represents the envelope of the probe field E_p, k_0 is the wavenumber, and $\Delta n(x)$ describes the distribution of the refractive index under the combined modulation of two partially overlapped EIT windows. According to Eq. (2), the intensity profiles of the output probe field under different two-photon detuning values can be obtained, and the dependence of the intensity ratio on two-photon detuning is shown by the solid line in Fig. 3(a), which indicates that with the increase of $|\Delta_p - \Delta_{c1(c2)}|$, the output diffraction intensity ratio gets larger accordingly. According to Eq. (1), with the growing of the two-photon detuning, both the real and the imaginary parts of the susceptibility will increase, leading to the improvement of the localization of light into each channel and the enhancement of the absorption in each channel, respectively. The improvement of the localization effect will lead to increased peak intensity inside each channel, while the presence of absorption can weaken the overall output intensity and plays a minor role in affecting the increasing trend of the output peak intensity. Actually, for a simple EIT system, the probe can experience stronger absorption (corresponding weaker output) when the two-photon detuning is set to far away from the resonance due to the Gaussian-like profile of the EIT window [24]. Here the increase of the output intensity for larger two-photon detuning
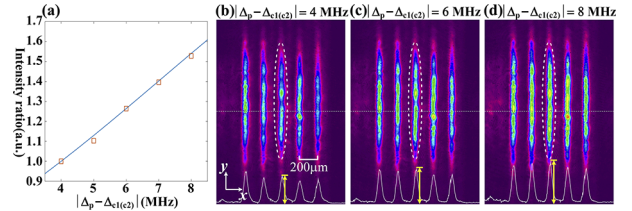
indicates the different properties of light in an anti-*PT* symmetric system compared to a simple EIT system. The intensity ratio is defined as the relative intensity of one selected bright fringe (marked by the ellipses in Figs. 3(b)–3(d)) on the output diffraction pattern under different two-photon detuning values divided by that of the same fringe at $|\Delta_p - \Delta_{c1(c2)}| = 4\,\text{MHz}$. In the experiment, by tuning the frequency of two AOMs and ECDL1 simultaneously to maintain the two-photon detuning condition of $(\Delta_p - \Delta_{c1}) = -(\Delta_p - \Delta_{c2})$, the anti-*PT*-symmetric photonic lattice with reconfigurable dispersion (Re[χ]) and loss (Im[χ]) can be experimentally constructed, and the experimental measured results are shown by the squares in Fig. 3(a), which is consistent with theoretical predictions. The observed output diffraction patterns under $|\Delta_p - \Delta_{c1(c2)}| = 4$, 6, and 8 MHz are depicted in Figs. 3(b)–(d), respectively, in which the white curve (from the software of the CCD camera) at the bottom of each figure shows the relative intensity of the region marked by the dashed line and the height of the peak represents the relative output intensity at each individual channel. As a consequence, the experimental results demonstrate that the photonic lattice we constructed is instantaneously adjustable and the distribution of the refractive index always maintains the anti-*PT*-symmetry under different two-photon detuning values.

In an anti-*PT* symmetric system, the evolution of the eigenvalues can be used to determine the non-Hermitian degree of the system [9,27]. Here we employ the coupling-mode theory to conduct a qualitative analysis of the anti-*PT*-symmetric system [33]:

$$i\begin{bmatrix} dE_i/dz \\ dE_j/dz \end{bmatrix} = \begin{bmatrix} -\alpha - i\gamma & i\kappa \\ i\kappa & \alpha - i\gamma \end{bmatrix}\begin{bmatrix} E_i \\ E_j \end{bmatrix}. \qquad (3)$$

The real part α and the imaginary part γ of the wave vector β correspond to the real and imaginary parts of the susceptibility, respectively, and κ is the coupling coefficient between two adjacent channels. According to Eq. (3), the Hamiltonian of the system can be obtained and the eigenvalues $\lambda_\pm = -i[\gamma \pm (\kappa^2 - \alpha^2)^{1/2}]$ can be analytically calculated. When $\kappa > \alpha$, the system lies in the anti-*PT*-symmetric phase, and the corresponding eigenvectors are $\psi_\pm = (\pm e^{\pm i\phi}, 1)^T$ with $\sin\phi = \alpha/\kappa$ [16]. So, the relative phase difference between supermodes in two adjacent channels varies from 0 to π continuously as the ratio α/κ changes under different two-photon detuning values. This is similar to that in a *PT*-symmetric system due to the formal equivalence of the eigenvectors [27], but the eigenvectors $\psi_\pm$ in the *PT*-symmetric system rely on the ratio γ/κ.

In the experiment, the behaviors of the eigenvectors can be reflected by the evolution of the relative phase difference between two adjacent channels. So, we introduce the reference
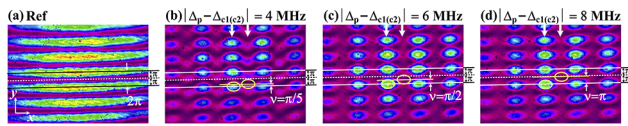
Fig. 4. (a) Reference interference. The distance between two adjacent fringes (marked by two solid lines) is defined as 2π, and the white dotted line represents the center of the two solid lines. (b)–(d) Measured phase differences ν between two adjacent channels (marked by two white one-way arrows, respectively) under the two-photon detuning $|\Delta_p - \Delta_{c1(c2)}| = 4$, 6, and 8 MHz, respectively, in which the solid yellow line marked the center of the dark region.

interference (interfering of two Gaussian beams, see Fig. 4(a)) to measure the relative phase difference between two adjacent bright and dark channels. Two solid lines marked the center of two adjacent bright fringes (along the y axis), and the distance is defined as 2π. The white dotted line is at the center of two solid lines, and its distance from each solid line is π. With the probe field being spatially discretized by the induced anti-PT-symmetric photonic structure, the reference interference pattern is transformed into a net-like square lattice (as shown in Figs. 4(b)–(d)), so that the phase difference between two adjacent channels can be measured by the relative shift along the y axis between the centers of the bright and dark spots (marked by two solid yellow circles). Considering that both the wave vector β and the coupling coefficient κ directly relate to the refractive index, the ratio α/κ in the above Hamiltonian can be tuned by varying the two-photon detuning $\Delta_p - \Delta_{c1(c2)}$, which can influence the relative phase between supermodes in two adjacent channels, as depicted in Figs. 4(b)–4(d). From these figures one can clearly see the relative phase that varies from $\pi/5$ to π, which reflects our constructed anti-PT-symmetric system that remains below the breaking threshold.

In theory, when the ratio α/κ decreases to exceptional point $\kappa = \alpha$, two eigenmodes degenerate with a relative phase of $\pi/2$. When $\kappa < \alpha$, the system undergoes a transition into the symmetry-broken phase and the eigenvectors are $\lambda_{\pm} = (ie^{\pm\phi}, 1)^{\mathrm{T}}$ with $\cosh\phi = \alpha/\kappa$, from which it is deduced that the relative phase difference remains locked at $\pi/2$. Since the symmetric breaking position (the region of energy bands degeneracy in Fig. 2(b)) is on the second and third energy bands, the excitation condition cannot be reached, and the fixed phase at $\pi/2$ (symmetry-breaking point) is not observed in the experiment.

In conclusion, we have experimentally demonstrated an anti-PT-symmetric photonic lattice under the EIT condition in a coherent three-level Λ-type ^{85}Rb atomic assemble. Such a photonic lattice can maintain an anti-PT symmetry under specific two-photon detuning condition, and the calculated band structure exhibits clear non-Hermitian features. The observed relative phase change between two adjacent bright and dark channels under the anti-PT symmetry is proved both theoretically and experimentally. Such an effectively controllable anti-PT-symmetric photonic lattice paves the way to investigate the unique beam dynamics in periodic anti-PT-symmetry optical potentials.

Disclosures. The authors declare no conflicts of interest.

REFERENCES

1. R. El-Ganainy, K. G. Makris, D. N. Christodoulides, and Z. H. Musslimani, Opt. Lett. **32**, 2632 (2007).
2. X. Wang and J. H. Wu, Opt. Express **24**, 4289 (2016).
3. L. Feng, R. El-Ganainy, and L. Ge, Nat. Photonics **11**, 752 (2017).
4. S. Klaiman, U. Gunther, and N. Moiseyev, Phys. Rev. Lett. **101**, 080402 (2008).
5. N. Wu, K. Cui, Q. Xu, X. Feng, F. Liu, W. Zhang, and Y. Huang, Sci. Adv. **9**, eabp8892 (2023).
6. K. G. Makris, R. El-Ganainy, D. N. Christodoulides, and Z. H. Musslimani, Phys. Rev. Lett. **100**, 103904 (2008).
7. L. Feng, M. Ayache, J. Huang, Y. Xu, M. Lu, Y. Chen, Y. Fainman, and A. Scherer, Science **333**, 729 (2011).
8. L. Chang, X. Jiang, S. Hua, C. Yang, J. Wen, L. Jiang, G. Li, G. Wang, and M. Xiao, Nat. Photonics **8**, 524 (2014).
9. C. E. Rüter, K. G. Makris, R. El-Ganainy, D. N. Christodoulides, M. Segev, and D. Kip, Nat. Phys. **6**, 192 (2010).
10. S. Longhi, Phys. Rev. Lett. **103**, 123601 (2009).
11. Z. Lin, H. Ramezani, T. Eichelkraut, T. Kottos, H. Cao, and D. N. Christodoulides, Phys. Rev. Lett. **106**, 213901 (2011).
12. Y. L. Chaung, A. Shamsi, M. Abbas, and Ziauddin, Opt. Express **28**, 1701 (2020).
13. J. H. Wu, M. Artoni, and G. C. La Rocca, Phys. Rev. Lett. **113**, 123004 (2014).
14. D. A. Antonosyan, A. S. Solntsev, and A. A. Sukhorukov, Opt. Lett. **40**, 4575 (2015).
15. Y. Li, Y. Peng, L. Han, M. Miri, W. Li, M. Xiao, X. Zhu, J. Zhao, A. Alù, S. Fan, and C. Qiu, Science **364**, 170 (2019).
16. F. Yang, Y. Liu, and L. You, Phys. Rev. A **96**, 053845 (2017).
17. S. Park, D. Lee, K. Park, H. Shin, Y. Choi, and J. W. Yoon, Phys. Rev. Lett. **127**, 083601 (2021).
18. V. V. Konotop and D. A. Zezyulin, Phys. Rev. Lett. **120**, 123902 (2018).
19. Q. Zhang, C. Yang, J. Sheng, and H. Wu, Proc. Natl. Acad. Sci. U. S. A. **119**, e2207543119 (2022).
20. P. Peng, W. Cao, C. Shen, W. Qu, J. Wen, L. Jiang, and Y. Xiao, Nat. Phys. **12**, 1139 (2016).
21. A. Bergman, R. Duggan, K. Sharma, M. Tur, A. Zadok, and A. Alu, Nat. Commun. **12**, 486 (2021).
22. C. Du, G. Wang, Y. Zhang, and J. H. Wu, Opt. Express **30**, 20088 (2022).
23. Y. He, J. Wu, Y. Hu, J. Zhang, and S. Zhu, Phys. Rev. A **105**, 043712 (2022).
24. J. Gea-Banacloche, Y. Li, S. Jin, and M. Xiao, Phys. Rev. A **51**, 576 (1995).
25. Z. Zhang, D. Ma, J. Sheng, Y. Zhang, Y. Zhang, and M. Xiao, J. Phys. B: At. Mol. Opt. Phys. **51**, 072001 (2018).
26. Z. Zhang, L. Yang, J. Feng, J. Sheng, Y. Zhang, Y. Zhang, and M. Xiao, Laser Photonics Rev. **12**, 1800155 (2018).
27. Z. Zhang, Y. Zhang, J. Sheng, L. Yang, M. A. Miri, D. N. Christodoulides, B. He, Y. Zhang, and M. Xiao, Phys. Rev. Lett. **117**, 123601 (2016).
28. J. Sheng, M.A. Miri, D. N. Christodoulides, and M. Xiao, Phys. Rev. A **88**, 041803 (2013).
29. S. Liang, Z. Liu, S. Ning, Y. Zhang, and Z. Zhang, Opt. Lett. **48**, 803 (2023).
30. Q. Yu, Z. Liu, D. Guo, S. Liang, Y. Zhang, and Z. Zhang, Nanomaterials **12**, 3222 (2022).
31. Y. Kang, H. Zhong, M. R. Belić, Y. Tian, K. Jin, Y. Zhang, F. Li, and Y. Zhang, Ann. Phys. **531**, 1900295 (2019).
32. Y. Zhang, D. Zhang, Z. Zhang, C. Li, Y. Zhang, F. Li, M. R. Belić, and M. Xiao, Optica **4**, 571 (2017).
33. Y. Choi, C. Hahn, J. W. Yoon, and S. H. Song, Nat. Commun. **9**, 2182 (2018).